

Received February 10, 2020, accepted February 28, 2020, date of publication March 3, 2020, date of current version March 12, 2020.

Digital Object Identifier 10.1109/ACCESS.2020.2977889

Slip-Aware Motion Estimation for Off-Road Mobile Robots via Multi-Innovation Unscented Kalman Filter

FANGXU LIU¹, XUEYUAN LI¹, SHIHUA YUAN¹, AND WEI LAN²

¹National Key Laboratory of Vehicular Transmission, Beijing Institute of Technology, Beijing 100081, China

²China North Vehicle Research Institute, Beijing 100072, China

Corresponding authors: Fangxu Liu (liufx13@gmail.com) and Wei Lan (w11976@163.com)

This work was supported by the National Key Research and Development Program of China under Grant 2017YFC0822202.

ABSTRACT Benefiting from high mobility and robust mechanical structure, ground mobile robots are widely adopted in the outdoor environment. The mobility of skid-steered mobile robots highly depends on the nonlinear and uncertain interaction between the tire and terrain. This paper introduces an approach to estimate the position, orientation, velocity, and wheel slip for the skid-steered mobile robots navigating on off-road terrains. More specifically, a Multi-Innovation Unscented Kalman Filter (MI-UKF) is developed to fusing different sensors' data. Historical innovations generated along the time sequence are merged into the update process of standard UKF to improve the accuracy of motion estimation. In the proposed estimator, an asymmetric ICR kinematic indicating wheel slip is taken into localization process. A four-wheeled prototype is introduced and three challenging test scenarios are designed. The improvements in orientation and velocity estimation are achieved according to results comparison. In the turning maneuver, the ICRs-based model operates more steady than the traditional wheel slip/skid model.

INDEX TERMS ICR kinematics, slippage estimation, skid-steered mobile robot, multi-innovation, unscented Kalman filter.

I. INTRODUCTION

Mobile robots are widely used in a variety of fields including in-door industries and out-door risky environments where high mobility is required. Among numerous types of mobile robots, skid-steered mobile robots (SSMR) are mostly applied as they are capable of traversing over various of terrains [1]. Particularly, wheeled skid-steered robots are mainly discussed for higher cruise speed and lower steering resistance than the tracked robots [2]. Even though many kinds of skid-steered robots are previously adopted in such fields like planetary exploration, military, agriculture, and construction, most of them are operated remotely. To release the human intervention in the mission and to extend other potential applications, there has been a growing interest in improving the autonomy of SSMRs.

Mechanically robust and simple for outdoor navigation as the SSMRs be, complex wheel/ground interaction makes it a challenging task to obtain an accurate kinematic and

The associate editor coordinating the review of this manuscript and approving it for publication was Okyay Kaynak¹.

dynamic model for the SSMRs. Significant wheel slip has been observed in outdoor navigating robots, such as Mars Rover [3], RobuROC6 [4], and CMU's Crusher [5]. Critical wheel slipping during the turning maneuver determines that the nominal kinematic model cannot describe the connection between wheel rotation and body motion. Understanding the information of wheel slip is essential for robot localization applications, such as dead reckoning (DR). On the other hand, the slip information directly decides the tractive and braking force that affect the robot's mobility and stability. Accurate position and velocity estimates are the basis of motion planning and tracking control [6], [7].

Wheel slip is the result of dynamic interaction between the wheel and terrain. Some variables such as longitudinal slip/skid, lateral skid, yaw speed, and lateral speed cannot be directly measured by sensors. State estimation algorithms such as Kalman filter (KF) or state observers are used in conjunction with multi sensors to derive estimates for parameters in kinematic or dynamic models [8].

The focus of this paper is to develop a multi-sensor fusion estimator to estimate the motion states including the position,

velocity, and wheel slip for the mobile robot navigating on the off-road ground. For a four-wheeled skid-steered mobile robot, we firstly discuss the kinematic model considering the wheel slip/skid by introducing a matrix consisting of the Instantaneous Center of Rotation (ICR) locations. Based on the asymmetric ICR kinematic model, we merge the historical innovations into the update process of UKF. Three experimental scenarios are designed to compare the proposed method with other estimators in position and velocity estimation. Results show that the MI-UKF performs more accurately especially for orientation and velocity estimation. Compared to the traditional wheel slip/skid definition, the ICR model acts more stably with less fluctuation.

The remaining sections of this paper are organized as follows. We start reviewing some related research work published in recent years in Section II. In Section III, we introduce the kinematic modeling of a skid-steered robot based on ICR locations and discuss several sensors adopted in the system. Section IV presents the design of a multi-innovation enhanced UKF estimator for localization and motion estimation. The experiments design and results comparison are presented in Section V. Finally, a conclusion and discussion of the future work are given in Section VI.

II. RELATED WORK

There has been substantial research into the problem of developing an effective and accurate motion estimator for Wheeled Mobile Robots (WMRs). The skid-steering locomotion poses a complex problem resulting in slippage as well as soil shearing and compacting. As proposed by Thrun [9], the same input would almost never produce the same results and the effects of robot actions were, therefore, best described as distributions. Eliazar and Parr [10] developed a probabilistic motion model to learn the motion model in SLAM application. The learning-based model was useful when the robot moves to an unknown terrain but asking for sophisticated parameter identification and tuning. The experiments-based method was also proposed [11], where the robot moved at low speed on soft terrain. And a plenty of researchers modeled the wheel motion by detecting the terrain properties. The terrain modeling is so complex that rare real-time applications are presented [39], [40].

In terms of the basic motion characteristics of the skid-steer, the robot actually behaves similar to tracked vehicles. So the methods of modeling tracked ground robots have been adopted to model the skid-steered mobile robot. In 2005, Martínez *et al.* [12] built a kinematic model for approximating the motion of tracked robots. The ICR-based model was first proposed. Later in 2017 [13], he improved the classic ICR model by taking the inertia force into account. In 2007, Mandow *et al.* [14] held that the ICR locations vary in bounded values related to vehicle dynamics. They built a Genetic Algorithm to identify the involved parameters. Experiments showed that the asymmetric ICR model presented higher accuracy in dead-reckoning. To simplify the model, Wang *et al.* [15] developed an ICR model under the

symmetric assumption and attributed investigation about the ICR parameters was conducted. Limited by the robot scale, the method was only tested at a low speed of 0.5m/s. In [16], Lu *et al.* established an ICR model based on six user-defined coefficients by that the lateral acceleration and path curvature were considered. More recently, Rabiee and Biswas [17] built an improved kinematic model merging the ICR location with the longitudinal slip rate of wheels on the basis of the friction model. The dynamic-based ICR model outperformed other methods in 6-s motion prediction.

For real-time applications, Kalman Filter (KF) and Extended Kalman Filter (EKF) were mostly utilized. In 2007, Yi *et al.* [18] developed an on-line KF estimator incorporating the wheel slip and velocity constraints to overcome the large drifting conducted by the integration of IMU measurement. The EKF estimator was also applied in Jिंगgang's work [19]. The indoor vision localization system was used to offering position reference. The sensing scheme consisting of GPS, IMU, and Encoder was getting popular in recent years [20]. In [21], a dynamic-model-based EKF was proposed with multi-sensors for wheel slip detection. The EKF estimate accuracy was improved by setting dynamic constraints. In 2012, Rogers-Marcovitz *et al.* [22] introduced a delayed state EKF to improve the odometry measurements used for vehicle navigation, but no explicit velocity and wheel slip information were offered. In 2014, Pentzer *et al.* [23] discussed the convergence of ICRs estimation using EKF. Thorough experiments for both a wheeled and a tracked robot were designed including circular path, curved path, long-distance traversal of 1km, the outage of GPS, and various speed and terrains. The estimation accuracy suffered from increasing navigating speed, longer distance, and conventional GPS. In [24], a hybrid scheme of EKF and KF was proposed to estimate the position and velocity of a 6-wheel skid-steered vehicle while only the longitudinal wheel slip was modeled. Recently, Wang *et al.* [25] introduced an innovation-based EKF combined with Bayesian filter for robot navigating on various terrains. A similar approach was introduced in [26], the process noise covariance was adjusted aided by terrain vision.

As discussed and analyzed by previous researchers [27], [41], EKF deals with the nonlinear system with Taylor extend, which will lead to accuracy reduction. UKF is beneficial from the sigma sampling and unscented transformation processes equipping with second-order accuracy while the Taylor extend only maintain first-order accuracy. Particle filter always results in high computational burden and its accuracy highly depends on the number of particles [28]. As a result, the UKF was believed more appropriate for the nonlinear kinematics of skid-steered mobile robots. More and more researchers adopted the UKF-based method in motion estimation for mobile robots and automated vehicles [29]. The standard UKF can be improved through combing with multi-innovation [30], [31], the historical innovations generated along the time. Multi-innovation theory was established by Ding and Chen [32]. The Multi-innovation-based

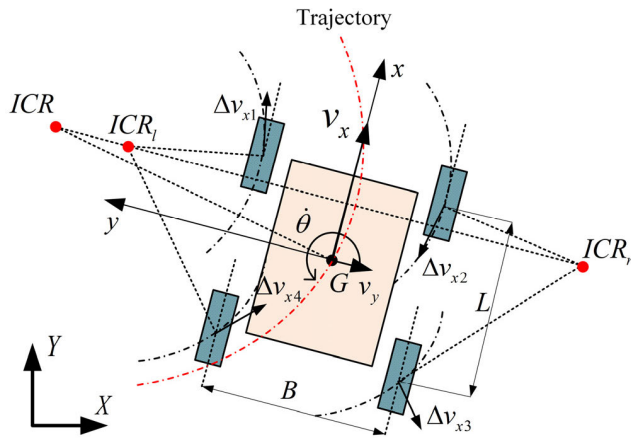


FIGURE 1. Top view of the skid-steered mobile robot.

identification has been applied with the least square method, stochastic gradient method and so on [33], [34]. But it is rarely utilized in the motion estimation of the mobile robot.

The contribution of our work is that we combine the multi-innovation theory with UKF and apply it in the motion estimation for high-speed off-road SSMRs. The pivotal motion states: position, heading, velocities, and wheel slip are estimated simultaneously. We design three test scenarios covering a high cruise speed of 4m/s, long distance of 100m, and large sideslip angle up to 40 degrees. According to the comparison of the results, the introduced MI-UKF obtains higher accuracy in the orientation and velocity estimation. What is more, it is also shown that the ICR model performs better in mapping the wheel slip/skid in turning maneuver.

III. SYSTEM MODELING AND PROBLEM STATEMENT

This section covers the kinematic modeling of a skid-steered mobile robot. Furthermore, the characteristics of onboard sensors and the motion analysis of driving in outdoor environment are discussed. The problem to be solved will be addressed at the end.

A. ICRS-BASED KINEMATIC AND MOTION ANALYSIS

To model a skid-steered mobile robot maneuvering on the ground, two coordinate frames are introduced, as shown in Fig. 1. The 2D world coordinate system (WCS) is defined as the X-Y, where the X-axis is the lateral axis of the inertia system. The origin of WCS is usually decided by the initial position of the robot at the beginning of a mission. The body coordinate system (BCS) with respect to the vehicle center of mass (CoM) is denoted by x-y, where the x-axis points to the body's longitudinal direction (forward) and the y-axis points to the left side of the vehicle. The longitudinal, lateral, and yaw velocities of the robot are represented by v_x , v_y and $\dot{\theta}$. In the BCS, the ICR location of the left wheels is defined as $ICR_l = (x_l, y_l)$. The ICR location of the right wheels is defined as $ICR_r = (x_r, y_r)$. The ICR location of the body is defined as $ICR = (x, y)$.

Four assumptions are declared for model simplification as follows [24],

- 1) The CG of robot locates on the geometric center of the body.
- 2) The robot navigates on the flat ground
- 3) The two wheels of each side rotate at the same speed
- 4) All the wheels are in contract with ground in same and constant radii when driving.

ICRs-based model is a widely adopted approach in the research of skid-steered vehicles, especially for mobile robots. Based on the assumptions built above, the rotation motion of wheels and body can be modeled based on ICRs' locations.

Specifically, the lateral coordinates of ICRs represent longitudinal skid or slipping of wheels. Let $\omega_i, i = 1, 2, 3, 4$ denotes the wheel angular velocities for front-left, rear-left, front-right and rear-right wheels respectively. From assumption 3), we have:

$$\omega_l = \omega_1 = \omega_2, \omega_r = \omega_3 = \omega_4 \quad (1)$$

Then the ICR locations are defined as follows,

Left ICR lateral location:

$$y_l = \frac{v_l - \omega_l r}{\dot{\theta}} + \frac{B}{2} = \frac{v_l + \frac{B}{2}\dot{\theta} - \omega_l r}{\dot{\theta}} = \frac{v_x - \omega_l r}{\dot{\theta}} \quad (2)$$

where, v_l and ω_l represent the linear speed and rotate speed of the left wheel center. r is the radii of the wheel and B is the wheel track.

Right ICR lateral location:

$$y_r = \frac{v_r - \omega_r r}{\dot{\theta}} - \frac{B}{2} = \frac{v_r - \frac{B}{2}\dot{\theta} - \omega_r r}{\dot{\theta}} = \frac{v_x - \omega_r r}{\dot{\theta}} \quad (3)$$

where, v_r and ω_r represent the linear speed and rotate speed of the right wheel center. In terms of the slipping and skidding of the wheel, the ICR locations perform as the following,

$$y_l \begin{cases} > \frac{B}{2}, & \text{slipping} \\ = \frac{B}{2}, & \text{pure rolling} \\ < \frac{B}{2}, & \text{skidding} \end{cases} \quad (4a)$$

$$y_r \begin{cases} > -\frac{B}{2}, & \text{slipping} \\ = -\frac{B}{2}, & \text{pure rolling} \\ < -\frac{B}{2}, & \text{skidding} \end{cases} \quad (4b)$$

The wheels and body are combined without relative motion, so the lateral coordinates of three ICRs are equal:

$$x_l = x_r = x = -\frac{v_y}{\dot{\theta}} \quad (5)$$

Apparently, with no lateral slipping, $x_l = x_r = x = 0$. Based on the ICR equations, the yaw speed can be calculated as:

$$\dot{\theta} = \frac{\omega_r r - \omega_l r}{y_l - y_r} \quad (6)$$

The longitudinal speed can be expressed as:

$$v_x = \frac{y_l \omega_r r - y_r \omega_l r}{y_l - y_r} \quad (7)$$

Combining Eq. (3), (4) and (5), the kinematics in BCS can be written as follows,

$$\begin{bmatrix} v_x \\ v_y \\ \dot{\theta} \end{bmatrix} = \begin{bmatrix} \frac{y_l \omega_r r - y_r \omega_l r}{\omega_r r - \omega_l r} \\ \frac{y_l - y_r}{\omega_r r - \omega_l r} x \\ \frac{y_l - y_r}{y_l - y_r} \end{bmatrix} = \mathbf{A}_{ICR} \begin{bmatrix} \omega_l r \\ \omega_r r \end{bmatrix} \quad (8)$$

where,

$$\mathbf{A}_{ICR} = \begin{bmatrix} \frac{-y_r}{y_l - y_r} & \frac{y_l}{y_l - y_r} \\ \frac{-x}{\omega_r r - \omega_l r} & \frac{y_l - y_r}{\omega_r r - \omega_l r} \\ \frac{-1}{y_l - y_r} & \frac{1}{y_l - y_r} \end{bmatrix}$$

In the WCS, the kinematics of the robot can be formulated via rotation matrix as:

$$\begin{bmatrix} \dot{X} \\ \dot{Y} \\ \dot{\phi} \end{bmatrix} = \begin{bmatrix} \cos \varphi & \sin \varphi & 0 \\ \sin \varphi & -\cos \varphi & 0 \\ 0 & 0 & 1 \end{bmatrix} \cdot \begin{bmatrix} v_x \\ v_y \\ \dot{\theta} \end{bmatrix} \quad (9)$$

The longitudinal and lateral slipping motion of wheels are indicated by matrix \mathbf{A}_{ICR} . The slipping kinematic model is supposed to be considered when navigating in outdoor environment. It turns to no-slip nominal kinematic model with the ICR locations of $x = 0, y_l = B/2, y_r = -B/2$. Given the traditional definition of the wheel slippage [35], the relationship can be depicted by following equations.

$$\begin{cases} s_l = \frac{2y_l - y_r}{y_l - y_r} \\ s_r = \frac{y_l - 2y_r}{y_l - y_r} \end{cases} \quad (10)$$

Moreover, ICR results can be used to obtain the slipping angle of the robot which follows the definition in [36]. As a result, the wheel slippage can be obtained when the ICR information is available.

B. SENSORS MODELING

A common multi-sensor scheme is adopted in our lab-designed robot, known as the incremental speed encoders, the IMU, the gyroscope and the dual antenna GNSS. Every sensor contributes to the final estimation results, so the analysis and modeling of their characteristics will be presented as follows.

1) ENCODER

The encoder is usually used to detect the rotation angle and speed mounting onto the output shaft of the electric motor. In this paper, the rotating speeds of the two-side motors

are measured. Following the nominal kinematics, the motion states of the robot can be obtained as follows,

$$\begin{bmatrix} v_x^{ICR} \\ v_y^{ICR} \\ \dot{\theta}^{ICR} \end{bmatrix} = \mathbf{A}_{ICR} \begin{bmatrix} \omega_l^{en} r \\ \omega_r^{en} r \end{bmatrix} \quad (11)$$

where, ω_l^{en} and ω_r^{en} represent the wheel rotating speed directly measured by encoders. i donates the reduction ratio of the reducer connecting the motor shaft and wheel. Lateral motion cannot be measured by the encoder since the wheels are fixed on the body with only longitudinal rolling feasible. The measurement consists of two parts, the nominal rotating speed and quantization error [37]. The quantization error is subjected to a uniform distribution $N(0, \mu)$, $\mu = 2\pi/\mu_0$, where μ_0 is the resolution of the encoder.

2) INERTIA MEASUREMENT UNION

The MEMS IMU consists of a gyroscope and an accelerometer providing angular speed and accelerations of three directions. In general, the systematic errors such as misalignment and scale factor inaccuracy can be calibrated in advance, so the random error will be considered in this paper. Two accelerations known as a_x^{imu} and a_y^{imu} and a yaw speed $\dot{\theta}^{imu}$ contribute to the robot velocities as follows,

$$\begin{bmatrix} v_x \\ v_y \\ \dot{\theta} \end{bmatrix} = \begin{bmatrix} v_{x,0} \\ v_{y,0} \\ \dot{\theta}^{imu} \end{bmatrix} + \begin{bmatrix} a_x^{imu} \\ a_y^{imu} \\ 0 \end{bmatrix} T \quad (12)$$

Practically, the accelerations and angular velocities retrieved from IMU are used to calculate state prediction as the system inputs.

3) DUAL ANTENNA GNSS

Global Navigation Satellite System can provide accurate localization supporting several navigation systems such as GPS, GLONASS, GALILEO and BeiDou. Typically, RTK GNSS can realize a high resolution of 0.01m in horizontal position and 0.005m/s in velocity. However, RTK GNSS requires local corrections that may not be available in all situations. Even though the Differential GNSS suffers from lower navigation accuracy of 0.3m in position, it is more widely utilized in autonomous navigation. GNSS satellite signals are very weak and struggle to penetrate through buildings and other objects obstructing view of the sky. GNSS can also occasionally drop out due to disturbances in the upper atmosphere. So the estimator is supposed to work robustly under the outage of GNSS information.

C. PROBLEM STATEMENT

For adaptive path planning and path tracking, the position, orientation and motion states are supposed to be calculated accurately. The state equation in this paper is expressed as follows,

$$v_{x,n+1} = v_{x,n} + a_x \Delta T \quad (13a)$$

$$v_{y,n+1} = v_{y,n} + a_y \Delta T \quad (13b)$$

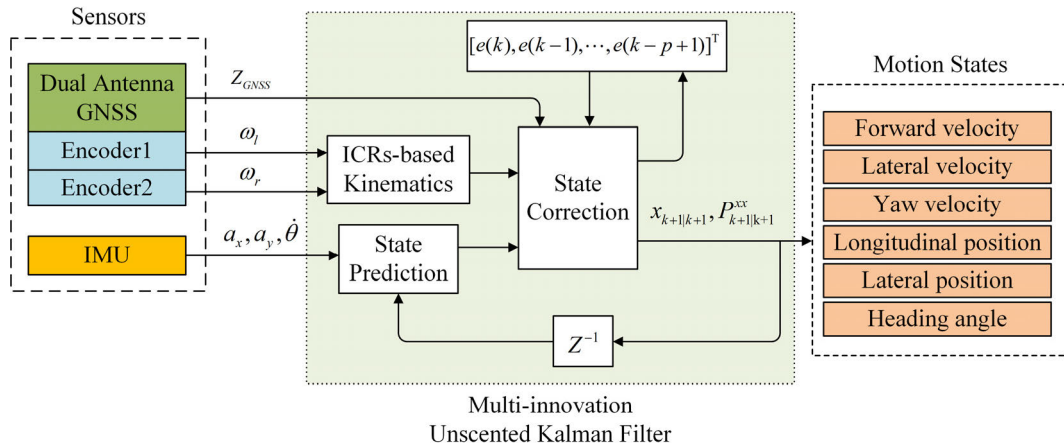


FIGURE 2. Structure of the proposed MI-UKF estimator.

$$\dot{\theta}_{n+1} = \dot{\theta}_n \tag{13c}$$

$$X_{n+1} = X_n + v_x \cos \varphi \Delta T + v_y \sin \varphi \Delta T \tag{13d}$$

$$Y_{n+1} = Y_n + v_x \sin \varphi \Delta T - v_y \cos \varphi \Delta T \tag{13e}$$

$$\varphi_{n+1} = \varphi_n + \dot{\theta} \Delta T \tag{13f}$$

We employ the combination of encoders and IMU to determine the position, orientation, and velocities of the robot by fusing their readings in the kinematic equation. Eq. (13a-c) represents the kinematics in BCS and Eq. (13d-f) represents the kinematics in WCS. First of all, the lateral velocity cannot be obtained through encoder’s reading. So the kinematic model including wheel slip information should be studied to map the relationship between body motion and wheel rotation. What’s more, the GNSS can also provide velocity measurements which is essential for the state update. As for the position estimation, once the motion state is generated, the position can be calculated by integration of velocities. In the long-distance traversal, the accumulative error can destroy the whole system. So the absolute position correction provided by GNSS is indispensable. Suffered from the low update rate and fragile signals, the GNSS data is not reliable constantly. So the estimator has to work robustly when the GNSS position is temporarily unavailable or when the GNSS provides drifting positions.

IV. LOCALIZATION AND MOTION ESTIMATION

In this section, we present the details of the motion estimation method that is used to estimate the following 6 states: X, Y, φ, v_x, v_y and $\dot{\theta}$ as shown in Eq. (13a-f). Even though other states like Z position, pitch angular speed, and roll angular speed can be measured by these sensors, we only take the mentioned states into account for system simplification.

In Part A, we outline the structure of the proposed motion estimator which is a multi-sensor and multi-innovation UKF. In Part B and C, we introduce the details of the multi-innovation UKF governing equations and implementation.

A. STRUCTURE OF PROPOSED ESTIMATOR

The motion estimation algorithm proposed in this paper uses a UKF combined with multi-innovations to achieve accurate and robust state estimate. The structure of the introduced estimator is shown in Fig. 2. The sensing system in this paper uses a Dual Antenna GNSS alongside with an IMU and two encoders mounted on two driven motors, which is a more standard approach for this category of off-road robots [24]. Furthermore, in the indoor and outdoor environment, it is most desirable to design an estimator accurately tracking the position only with proprioceptive sensors such as encoders and IMU. The fact that errors will accumulate if there are no exteroceptive sensors to correct localization makes the GNSS indispensable in outdoor applications, especially on a long journey. As a result, some researchers proposed a hierarchical estimator using several KFs [24].

In terms of the estimator introduced in this paper, we adopted an integrated estimation system promising the data reading of GNSS can be merged into the update process whenever the GNSS data is available. Normally, all the sensors are assumed working well to obtain effective ICR parameters via MI-UKF. The IMU data ($a_x, a_y, \dot{\theta}$) is the system input of the state prediction process. The predicted states then are corrected following the MI-UKF algorithm when the encoder and GNSS data are available. Then the ICR parameters (y_l, y_r, x) can be generated to build the ICR kinematic model. More details about the MI-UKF will be discussed in the next section. Once the GNSS data is blocked or deviated, the previous GNSS data still takes effect in the estimate results through ICR kinematics.

B. MULTI-INNOVATION UKF FUSION METHOD

1) REVIEW OF UKF

The UKF algorithm is a filtering algorithm for the nonlinear system, differing from the EKF algorithm. In UKF, the sigma sampling process and unscented transition are adopted to present the nonlinear characteristics of the system instead of linearization. The state transition equation

and measurement equation of the dynamic system can be expressed as follows:

$$\begin{cases} x_{k+1} = f(x_k, u_k, w_k) \\ z_{k+1} = h(x_{k+1}, u_k, v_k) \end{cases} \quad (14)$$

where x_{k+1} donates the predicted state of the $(k + 1)$ th sampling period of the system from the (k) th estimated state, and z_{k+1} donates the predicted observation of the $(k + 1)$ th sampling period based on the predicted state. The function $f(\cdot)$ donates the state transition function and $h(\cdot)$ donates the observation function. w_{k+1} and v_{k+1} represent the process noise and measurement noise respectively.

The standard unscented Kalman filter algorithm is calculated as following:

- 1) Initializing the state and corresponding covariant matrix:

$$\begin{cases} \hat{x}_0 = E(x_0) \\ P_0 = E[(x_0 - \hat{x}_0)(x_0 - \hat{x}_0)^T] \end{cases} \quad (15)$$

- 2) Sigma sampling of state vector and calculating the weights of sampling points and covariant:

$$x_{k|k}(i) = \begin{cases} \hat{x}_k, & i = 1 \\ \hat{x}_k + \sqrt{(n + \lambda)P_{k|k}}, & i = 2, \dots, n + 1 \\ \hat{x}_k - \sqrt{(n + \lambda)P_{k|k}}, & i = n + 2, \dots, 2n + 1 \end{cases} \quad (16)$$

$$W_k(i) = \begin{cases} \frac{\lambda}{n + \lambda}, & i = 1 \\ \frac{1}{2(n + \lambda)}, & i \neq 1 \end{cases} \quad (17)$$

$$W_c(i) = \begin{cases} \frac{\lambda}{n + \lambda} + (1 - \alpha^2 + \beta), & i = 1 \\ \frac{1}{2(n + \lambda)}, & i \neq 1 \end{cases} \quad (18)$$

where n is the dimension of the state vector. $\lambda = \alpha^2(n + k) - n$, $\alpha \in [0, 1]$ donates the discreteness of the sampling points. $\beta = 2$ and $k = 0$ are defined in the nominal distribution.

- 3) Unscented transition of system state matrix and covariance calculation

$$\begin{cases} x_{k+1|k}(i) = f(x_{k|k}(i), u_k) \\ \hat{x}_{k+1|k} = \sum_{i=1}^{2n+1} W_k(i)x_{k+1|k}(i) \end{cases} \quad (19)$$

$$P_{k+1|k} = \sum_{i=1}^{2n+1} W_c(i)(x_{k+1|k}(i) - \hat{x}_{k+1|k}) \times (x_{k+1|k}(i) - \hat{x}_{k+1|k})^T + Q_{k+1} \quad (20)$$

- 4) Unscented transition of system state matrix and covariance calculation

$$\begin{cases} z_{k+1|k}(i) = h(x_{k+1|k}(i), u_{k+1}) \\ \hat{z}_{k+1|k}(i) = \sum_{i=1}^{2n+1} W_k(i)z_{k+1|k}(i) \end{cases} \quad (21)$$

$$P_{k+1|k} = \sum_{i=1}^{2n+1} W_c(i)(z_{k+1|k}(i) - \hat{z}_{k+1|k}) \times (z_{k+1|k}(i) - \hat{z}_{k+1|k})^T + R_{k+1} \quad (22)$$

- 5) Calculation of the Kalman gain and covariance between predicted states and measurements

$$\begin{cases} P_{k+1|k}^{xz} = \sum_{i=1}^{2n+1} W_c(i)(x_{k+1|k}(i) - \hat{x}_{k+1|k}) \\ (z_{k+1|k}(i) - \hat{z}_{k+1|k})^T \\ K_{k+1} = P_{k+1|k}^{xz} P_{k+1|k}^{zz}^{-1} \end{cases} \quad (23)$$

- 6) Update of the state variable and the covariance

$$\begin{cases} x_{k+1|k+1} = \hat{x}_{k+1|k} + K_{k+1}(z_{k+1} - \hat{z}_{k+1|k}) \\ P_{k+1|k+1} = P_{k+1|k} - K_{k+1} P_{k+1|k}^{zz} K_{k+1}^{-1} \end{cases} \quad (24)$$

2) MULTI-INNOVATION ENHANCED UKF

Almost the previous identification methods and filtering algorithms known as Least Square Method, Stochastic Gradient Method, and Kalman Filters are based on single innovation modification (SIM). In recursive algorithm, innovation indicates the prediction error of system, expressed as:

$$e_{k+1} = z_{k+1} - h(\hat{x}_k) \in \mathbb{R}. \quad (25)$$

where z_{k+1} is the observation at $(k + 1)$ time, \hat{x}_k is the estimation at (k) time. Different from the residuals, innovation represents the prediction error. By collecting historical identification innovations and all eigenvalues of state equation included in unit circle, the convergence accelerates and accuracy are enhanced.

According to Multi-Innovation theory [32], the innovation length p is defined, and the innovation variable in Eq. (25) is extended as innovation vector named multi-innovation:

$$\mathbf{E}(p, k + 1) := \begin{bmatrix} e_{k+1} \\ e_k \\ \vdots \\ e_{k+2-p} \end{bmatrix} = \begin{bmatrix} z_{k+1} - h^{k+1}(\hat{x}_{k+1}) \\ z_k - h^k(\hat{x}_k) \\ \vdots \\ z_{k+2-p} - h^{k+2-p}(\hat{x}_{k+2-p}) \end{bmatrix} \quad (26)$$

Meanwhile, the Kalman gain is extended as gain matrix:

$$\mathbf{K}_{k+1}^p = [K_{k+1}^1, K_{k+1}^2, \dots, K_{k+1}^p] \in \mathbb{R}^{n \times p} \quad (27)$$

where K_{k+1}^p represents the Kalman gain at $(k + 2 - p)$ time. So update process of standard UKF is enhanced as:

$$\begin{cases} x_{k+1|k+1} = \hat{x}_{k+1|k} + \sum_{i=1}^p \lambda_i K_{k+1}^i (z_{k+2-i} - h^{k+2-i}(\hat{x}_{k+2-i})) \\ P_{k+1|k+1} = P_{k+1|k} - K_{k+1}^1 P_{k+1|k}^{zz} K_{k+1}^1^{-1} \end{cases} \quad (28)$$

In this case, the MI-UKF can be degenerated to standard UKF when $\lambda_2 = \lambda_3 \dots = \lambda_p = 0$. Not only the measurement at time $(k - 1)$ contributes but the measurements at times $(k - i)$ are taken into consideration in MI-UKF.

In previous work, Xie et al. [38] discussed the performance of KF with fading factors and raised that accumulative interference may occur if the effect of old measurements and new measurements both are equally weighted. According to the research of Liu et al. [30], the influence of new measurement should be greater than that of old measurements. The maximum gain weight at the present time is guaranteed as follows,

$$\begin{cases} \lambda_1 = 1 \\ \lambda_2 = \lambda_3 \dots = \lambda_p = \frac{a}{p-1}, 0 \leq a \leq 1 \end{cases} \quad (29)$$

where a is an adjustable coefficient set as $a = 0.5$.

In general, the more innovations are added in the Kalman filter, the better performance can be obtained. The definitive parameters like innovation length and Kalman gain weight play a very important role in ensuring the performance of MI-UKF. Considering the trade-off between computation burden and estimation precision, the innovation length is set as 2.

C. DISCRETE KINEMATIC MODEL

To implement the MI-UKF, we rewrite the state equations in Eq. (14) following the MI-UKF algorithm, where the observation equations are sampled at each time interval.

$$\mathbf{x}_{k+1} = \mathbf{f}(\mathbf{x}_k, \mathbf{u}_k) + \mathbf{w}_k \quad (30)$$

where,

$$\mathbf{f}(\mathbf{x}_k, \mathbf{u}_k) = \begin{bmatrix} X_k + v_{x,k} \cos \varphi_k \Delta T + v_{y,k} \sin \varphi_k \Delta T \\ Y_k + v_{x,k} \sin \varphi_k \Delta T - v_{y,k} \cos \varphi_k \Delta T \\ \varphi_k + \dot{\theta}_k \Delta T \\ v_{x,k} \\ v_{y,k} \\ \theta_k \end{bmatrix}$$

State vector $\mathbf{x}_k = (X_k, Y_k, \varphi_k, v_{x,k}, v_{y,k}, \dot{\theta}_k)$, and the noise vector $\mathbf{w}_k = (\sigma_1, \sigma_2, \sigma_3, a_{x,k} \Delta T, a_{y,k} \Delta T, \sigma_4)$. $(a_{x,k}, a_{y,k})$ is the IMU measurement at the (k) sampling time, acting as the input of the system, and ΔT is the data-sampling period.

The observation vector $\mathbf{z}_{k+1} = (\mathbf{z}_{GNSS}, \mathbf{z}_{Encoder})^T$ consists of absolute position, orientation and velocity measured by GNSS and Encoder. The measurement equation sampled at $(k + 1)$ sampling time can be written as,

$$\mathbf{z}_{k+1} = \mathbf{h}(\mathbf{x}_{k+1}) + \mathbf{v}_{k+1} \quad (31)$$

where $\mathbf{h}(\mathbf{x}_{k+1})$ and the measurement noise vector \mathbf{v}_{k+1} are listed in Appendix. On the basis of sensors modelling discussed in Section III, the measurement vector consisting of

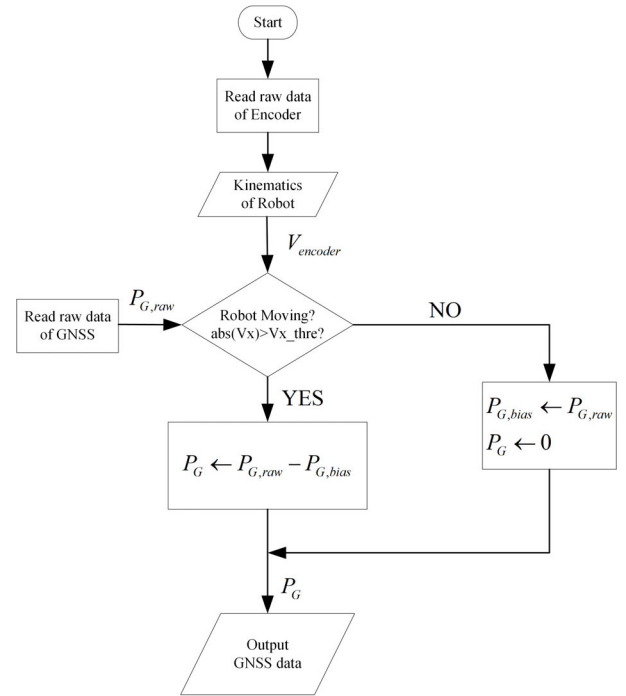


FIGURE 3. Flow chart of the zero drifting removal algorithm.

GNSS and Encoder reading is written as:

$$\mathbf{z}_{k+1} = \begin{bmatrix} N_{k+1} \sin \varphi_{N,k+1} + E_{k+1} \cos \varphi_{N,k+1} \\ N_{k+1} \cos \varphi_{N,k+1} - E_{k+1} \sin \varphi_{N,k+1} \\ \varphi_{k+1} \\ v_{N,k+1} \sin \varphi_{N,k+1} + v_{E,k+1} \cos \varphi_{N,k+1} \\ v_{N,k+1} \cos \varphi_{N,k+1} - v_{E,k+1} \sin \varphi_{N,k+1} \\ \dot{\theta}_{k+1} \\ X_k^{ICR} \\ Y_k^{ICR} \\ \varphi_k^{ICR} \\ v_{x,k+1}^{ICR} \\ v_{y,k+1}^{ICR} \\ \dot{\theta}_{k+1}^{ICR} \end{bmatrix} \quad (32)$$

where $(X_k^{ICR}, Y_k^{ICR}, \varphi_k^{ICR}, v_{x,k+1}^{ICR}, v_{y,k+1}^{ICR}, \dot{\theta}_{k+1}^{ICR})^T$ is presented in Appendix.

In the case that the measurements of GNSS are faulty or unavailable, the dimension of the measurement vector will descend to 9×1 with the position readings deleted. Theoretically, GNSS can provide the locations and velocities with high resolution. However, the GNSS system inevitably suffers from many shortcomings mentioned before which may pollute the estimation results leading to system crash. One typical condition considered in this paper is zero drifting (random walking), which occurs in the initiative time. Zero drifting will cause localization deviation in the whole term. As shown in Fig. 3, an algorithm runs to get rid of the zero drifting when the GNSS system initiates. With lower drifting error, the encoders are used to detect if the robot is moving so that the zero drifting error of GNSS can be calculated and

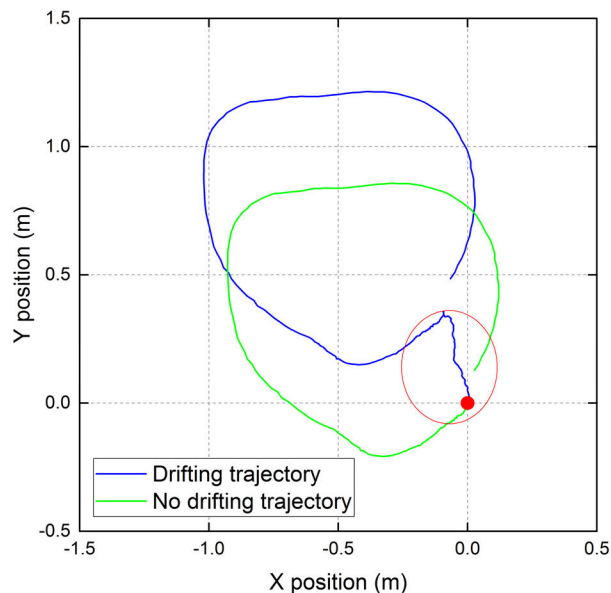


FIGURE 4. Zero drifting removal results.



FIGURE 5. The experimental platform DUBHE and Experimental flat dirt ground.

cut off. As shown in Fig. 4, the trajectory in blue shows the robot's locations with zero drifting while the green line is the corrected result by running the proposed algorithm.

V. EXPERIMENT AND ANALYSIS

This section describes experimental tests set to verify the effectiveness of the proposed MI-UKF estimator. First of all, the test platform designed by our lab is introduced. Then, three driving scenarios are presented to compare the performance of the proposed method with other previous ones.

A. EXPERIMENT SET-UP

The robot platform illustrated in Fig. 5 is a four-wheeled skid-steered robot named DUBHE designed by Vehicle Research Lab of BIT. The main configurations of the platform

TABLE 1. Parameters of the platform DUBHE.

Parameter	Value	Description
B	0.87m	Wheel track
L	0.79m	Wheel base
r	0.23m	Radius of wheel
m	200kg	Mass of robot
v_m	9m/s	Maximum cruise speed
R_{min}	0m	Minimum steer radius
P_{rate}	1.8kW	Rate power of motor
n_{rate}	3000r/min	Rate speed of motor

are listed in Table. 1. Two servo motors equipped with encoders are mounted on the two sides of the robot while the wheels of each side are transmitted by belt to promise the same speeds. The robot is designed to be symmetrical in terms of the locations of battery and computer. The symmetrical weight distribution results in a CoM at the geometric center of the body. IMU is located on the CoM of the body so that the calibrations of the IMU bias for state estimation can be ignored. The antennas are placed along the longitudinal direction of the body. Perception sensors like RGB-D camera and VLP-16 lidar are mounted on the body for environment mapping and recognition. Designed for the outdoor implementation, the platform can drive with a maximum speed of 9m/s. Limited by the fixed suspension, the platform normally drives up to 4m/s which already satisfies our research in high-speed navigation of the mobile robots.

In this research, field experiments arranged as straight path cruise, large radius turning and small radius turning are performed on the flat dirt ground. Details about estimated position, orientation, velocity and wheel slipping results for the test scenarios will be discussed in the following sections.

B. SCENARIO 1: STRAIGHT PATH

As for the straight path scenario, the longitudinal speed and yaw speed are set as 4m/s and zero respectively, and the robot is remotely controlled by joystick.

1) POSITION AND ORIENTATION ESTIMATES

Driving in the open area, the GNSS reading is assumed to be accurate enough to be the reference in this test. As shown in Fig 6, five different position results are presented. The robot starts from the red point, and its initial heading angle is 1.18. The trajectory is not a perfectly straight line as the result of uneven road and wheel slip. The black dot line on the plot shows the GNSS solution of the robot position. The most common dead-reckoning (DR) localization for the test platform is drawing as a dot line in gray employing only

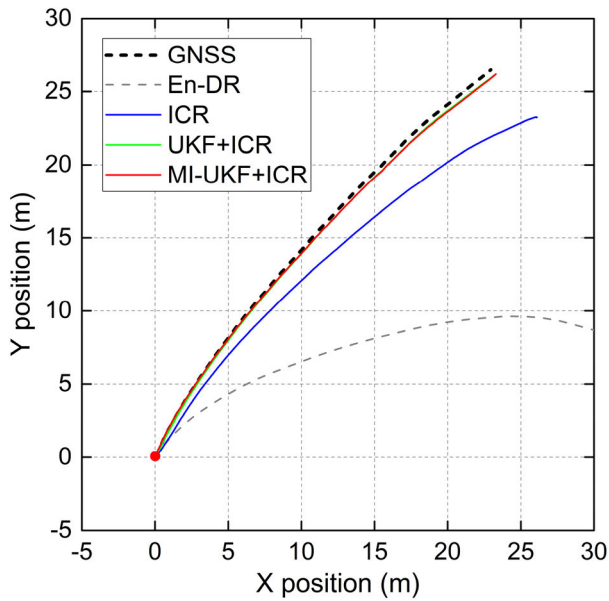


FIGURE 6. XY position estimation driving on a straight path.

encoder data to calculate the position based on the no-slip kinematic model. The blue line represents the results of only ICR kinematic model but without GNSS reading. Then, by adding GNSS measurements, the results can be further improved as shown in the green line. As for the red line, the trajectory generated by the MI-UKF estimator lies close enough to the GNSS solution.

Contributions rely on the ICR measurement model as well as the MI-UKF algorithm. Taking the GNSS position as reference, the En-DR result shows an obvious gap caused by unmodeled wheel slip and ground uncertainty. Much improvement is achieved when the ICR model is considered into the UKF update equation. However, without absolute position correction, the accumulated error is still too much to adopt in robot navigation in a long distance. As it shows in Fig. 6, the result of UKF+ICR performs much better than ICR solution. And in this scenario, the proposed MI-UKF estimator just performs much close to the UKF-ICR in terms of localization estimation. Generally, on a straight path, the improvement magnitude of MI-UKF is less than that of the slip-aware ICR model.

In addition, Fig. 7 shows the orientation estimation of the robot using the different methods mentioned above. Because the chassis controller did not take the wheel slip into account and the ground is uneven to some extent, the actual orientation changes from 1.18 to 0.67. The MI-UKF estimator can track the GNSS orientation very closely comparing to the other two methods. Without considering the wheel slipping, the En-DR may suffer a bad estimation of orientation, which is a major factor resulting in position error in a long-distance traversal.

2) VELOCITY ESTIMATES

The estimated velocity of the experimental platform in BCS is shown in Fig. 8. Subfig8(a), (b), and (c) illustrate the SSMR's longitudinal speed, lateral speed, and yaw speed respectively.

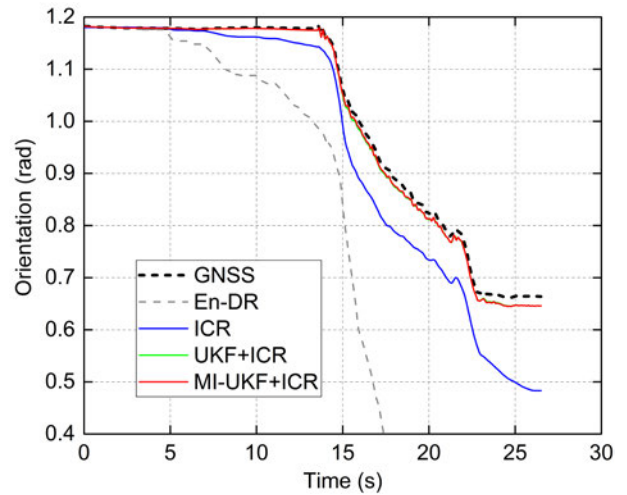


FIGURE 7. Orientation estimation during driving on a straight path.

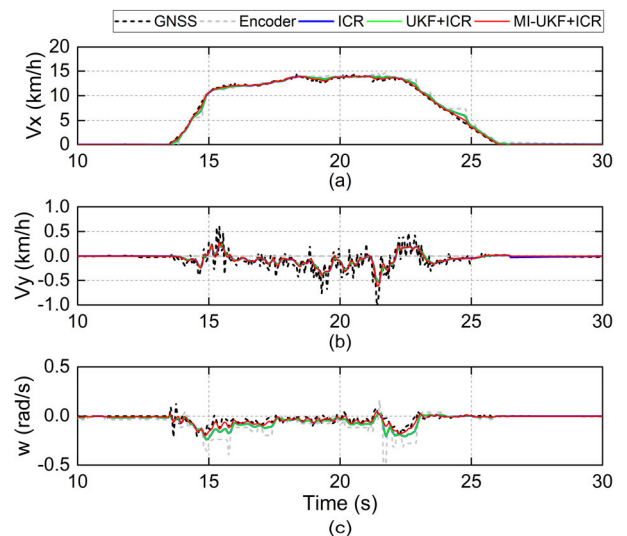


FIGURE 8. Navigating speeds of robot during driving on a straight path.

Similarly, there are five different results in velocity estimates. The robot accelerates at 14s and reaches the desired speed at 15s. The stationary speed is about 4m/s. In the straight path scenario, nearly no offset is shown in longitudinal speed estimates. This is because the wheel rotates with no longitudinal slip when driving straight and steady. Even so, lateral slipping does happen, which cannot be measured by encoders wherein its reading is zero. The lateral speed estimates are more relevant to the GNSS measurements. The yaw speed estimates show more differences among estimators. The encoder solution is obviously higher than others which will accumulate higher orientation error. Since it is more apparent when accelerating and decelerating, the estimated lateral speed and yaw speed can be considered as disturbances in the controller design.

3) LONGITUDINAL AND LATERAL SLIP

In a computing period time, the wheel rotating speeds and robot navigating speeds are used to calculate the wheel's slipping motion.

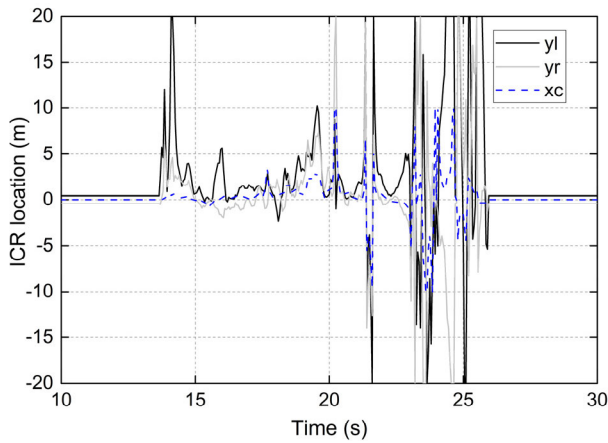


FIGURE 9. ICR estimates during driving on a straight path.

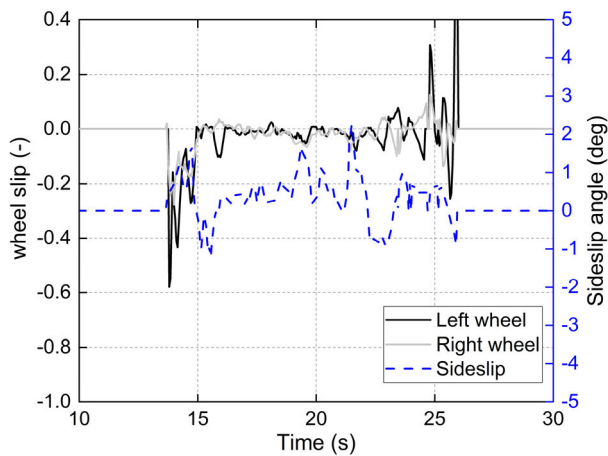


FIGURE 10. Wheel slip rate of the robot during driving on a straight path.

Based on the ICR kinematic model discussed before, the ICR locations are illustrated in Fig. 9. The initial ICR locations are 0.435m, -0.435m, and 0m. Accordingly, we can hold that the left wheel is in slipping condition most of the time while the right wheel is skidding. It is necessary to mention that the ICR locations fluctuate significantly when accelerating and decelerating. This is not only because of the wheel slip as shown in Fig. 10, but also the result of little yaw speed acting as a denominator in ICR expressions. Proposed by previous research [12], [23], the ICR locations may reach infinity so it is restrained in $[-20, 20]$ in our work. As shown in Fig. 10, the longitudinal slip is relatively small from 16s to 22s while the ICR locations fluctuate up to 10m. Consequently, the ICR model performs poorly in the straight path navigating unless proper constrains or methods are introduced.

C. SCENARIO2: CURVED PATH WITH LARGE RADIUS

This section presents the condition that the robot driving on the curved path with a radius around 17m, a more realistic driving scenario in the real application of the outdoor mobile robot. The desired longitudinal speed is set as 3m/s, and the desired yaw speed is about 0.5rad/s.

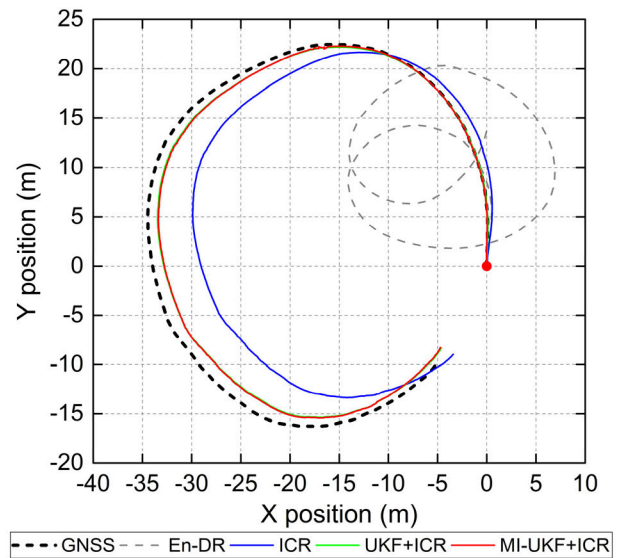


FIGURE 11. XY position estimation during driving on curved path with large radius.

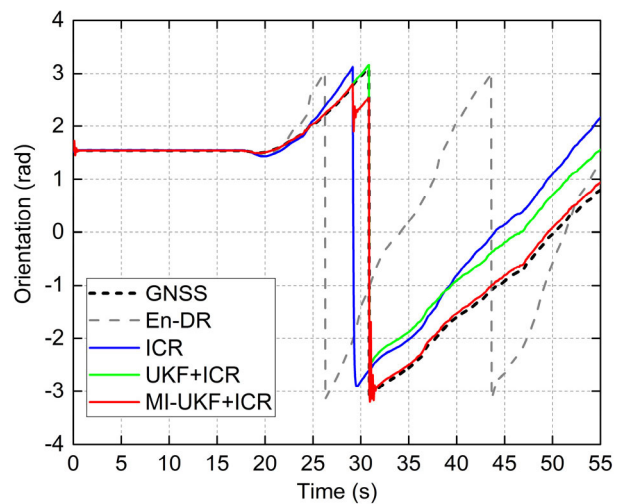


FIGURE 12. Orientation estimation during driving on curved path with large radius.

1) POSITION AND ORIENTATION ESTIMATES

The position estimate results are shown in Fig. 11. In this scenario, the robot travels a relatively long journey about 100 meters in a circular path. With the same trend in Scenario 1, the ICR-included results perform similarly while the results of En-DR totally deviates from a radius of about 10m. The proposed MI-UKF can realize an accurate estimate at the early stage but the difference between GNSS and MI-UKF over 100m of traversal is within 1m. In addition, the orientation estimates are presented in Fig. 12. As defined before, the orientation angle is restrained in $[-\pi, \pi]$. The significant improvement conducted by ICR model can be seen by comparing the ‘ICR’ trajectory with ‘En-DR’ trajectory. And the improvement conducted by multi-innovation can be seen by comparing the ‘MI-UKF’ result and ‘UKF’ result. The integral graph of four different methods introduced a clear

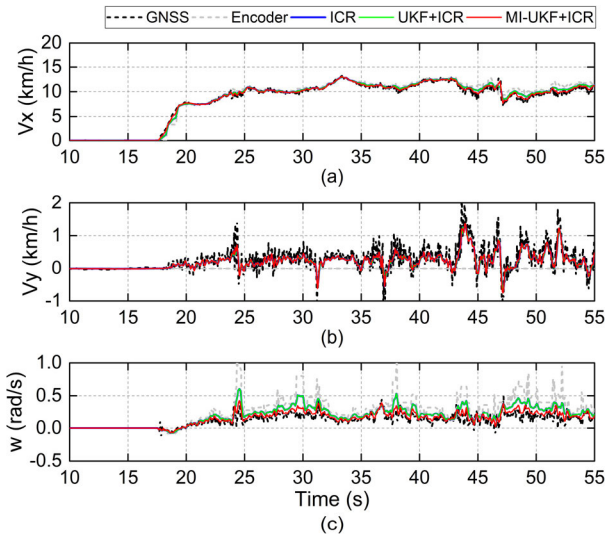


FIGURE 13. Navigating speeds of robot during driving on curved path with large radius.

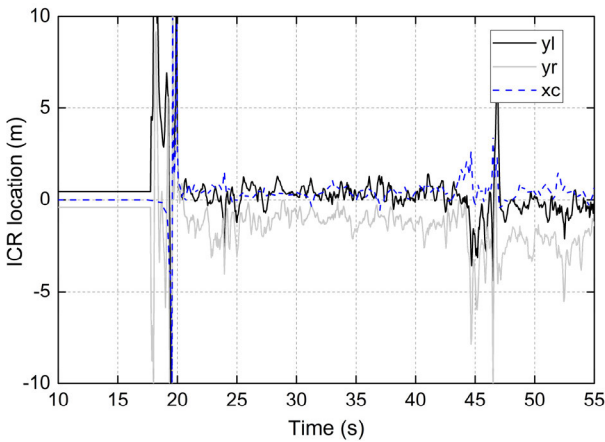


FIGURE 14. ICR estimates during driving on a curved path with large radius.

improvement trend. The proposed MI-UKF performs in the highest accuracy in heading estimation.

2) VELOCITY ESTIMATES

The velocity estimate results of moving on a curved path over 100m are shown in Fig. 13. Subfig13(a), (b), and (c) illustrate the SSMR’s longitudinal speed, lateral speed, and yaw speed respectively. The results in the early 10 seconds when the robot is not moving are cut off for better illustration. The differences in longitudinal speed estimates are noticeable among these methods. The other four resolutions are slightly lower than the encoder’s reading since the wheel is slipping. According to the lateral speeds, we can see the robot is skidding laterally in the opposite direction of the y-axis. The actual yaw speed is below 0.5 rad/s due to the lateral skidding. The yaw speed calculated through MI-UKF is closer to the GNSS measurement than that of other methods.

3) LONGITUDINAL AND LATERAL SLIP

Fig. 14 shows the ICR locations estimates for the robot navigating on a curved path with a large radius. The ICR locations

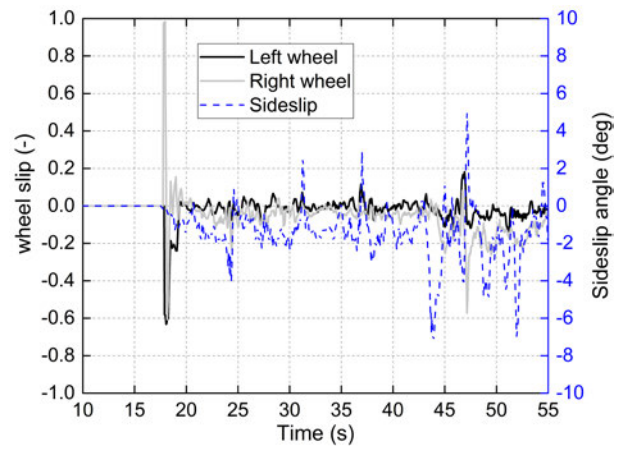


FIGURE 15. Wheel slip rate of the robot during driving on a curved path with large radius.

fluctuate critically at 17s-20s when the robot is accelerating. During the stationary steering motion, the means of the ICR locations are 0.333m, $-1.168m$, and $0.391m$ respectively. Compared to the results in scenario 1, the ICR estimates are more stable at higher yaw speed in scenario 2. The wheel slip rate is shown in Fig. 15. In this scenario, the maximum slipping rate is up to -20% , where ‘ $-$ ’ represents the right wheel is skidding. From the slipping rate curve, we can point out that the right wheel skids more critically than the left wheel, which is consistent with the ICR estimate results. Moreover, the ICR locations look more stable than the slip rate curve, especially for the sideslip motion.

D. SCENARIO3: CURVED PATH WITH SMALL RADIUS

One major advantage of the skid-steered robot is that it can steer in a very small radius even in zero. This mobility promises the robot navigating in a challenging environment. In this scenario, the desired longitudinal speed is set as $-1m/s$, and the desired yaw speed is about $-2 rad/s$. That means the robot is driving backward with a very small radius of $0.4m$.

1) POSITION AND ORIENTATION ESTIMATES

The position estimates comparison under the small-radius steering is shown in Fig. 16. The trajectory generated by En-DR is a perfect circle, while the actual trajectory measured by GNSS indicates that the robot is skidding outside generating a larger and un-round circle. The significant improvement conducted by ICR model can be seen by comparing the ‘ICR’ trajectory with ‘En-DR’ trajectory. And the improvement conducted by multi-innovation can be seen by comparing the ‘MI-UKF’ result and ‘UKF’ result. Meanwhile, obvious chattering occurs in the MI-UKF result when the robot’s orientation changes from $-\pi$ to π . The phenomenon is more noticeable in Fig. 17 where the orientation estimates are shown. This is because historical innovations are merged into the UKF process leading to chattering when the state variable is discontinuous. In this case, by modifying the orientation

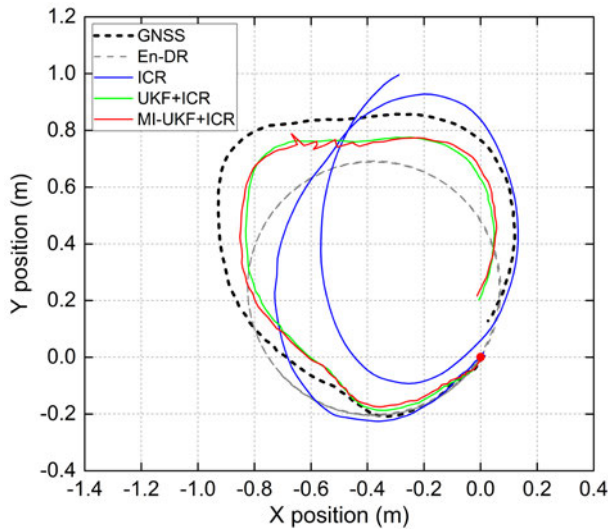


FIGURE 16. XY position estimation during driving on curved path with small radius.

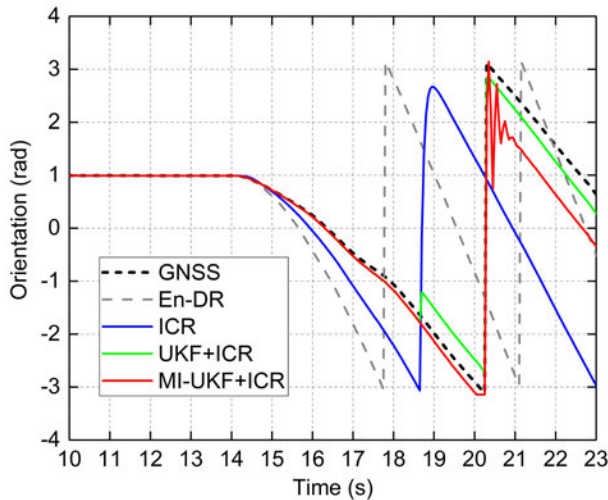


FIGURE 17. Orientation estimate during driving on curved path with small radius.

angle as a monotonically increasing value, the chattering can be eliminated, as shown in Fig. 7 in scenario 1.

2) VELOCITY ESTIMATES

The navigating speed of the robot steering in a small radius is presented in Fig. 18. Subfig18(a), (b), and (c) illustrate the SSMR’s longitudinal speed, lateral speed, and yaw speed respectively. The longitudinal speed estimates in this scenario are much different from those before. The desired velocity is -1m/s while the GNSS measures only -0.3m/s . The proposed MI-UKF suggests that the longitudinal speed is -0.5m/s which is close enough to the GNSS measurement. What is more important is the lateral speed is up to 0.4m/s , even higher than the longitudinal speed in sometimes. This is a common condition for the skid-steered robot when steering in a small radius. Various yaw speed estimates are also produced. The actual value is considered as -1rad/s measured by GNSS and MI-UKF. Generally, the velocity estimation

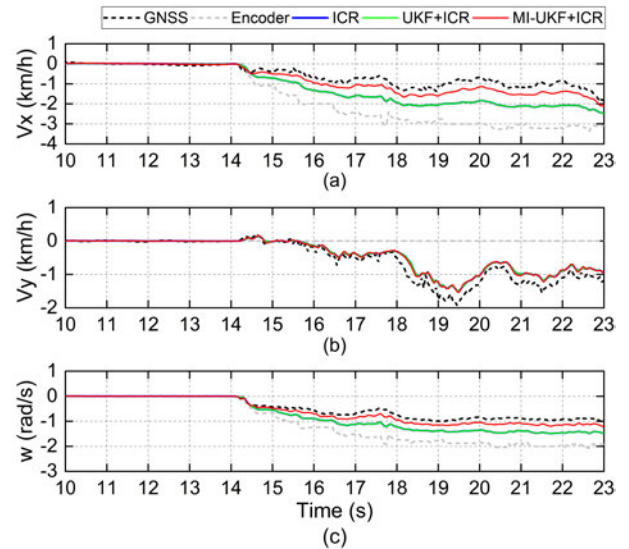


FIGURE 18. Navigating speed of the robot driving on a curved path with small radius.

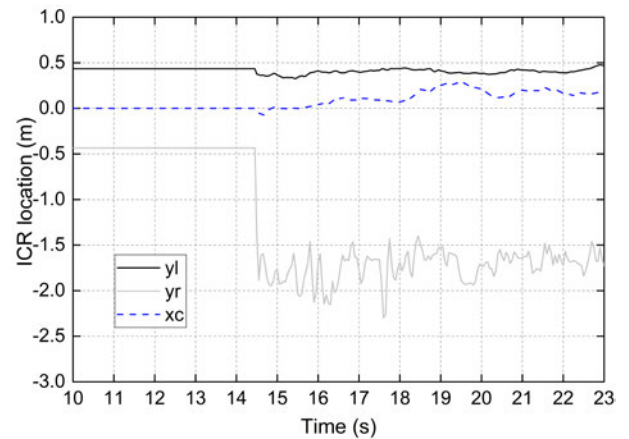


FIGURE 19. ICR estimates during driving on a curved path with small radius.

varies a lot among the four different methods where high longitudinal and lateral slip occur.

3) LONGITUDINAL AND LATERAL SLIP

The ICR locations estimates of the robot steering in a small radius are shown in Fig. 19. Different from the two scenarios discussed before, the ICR locations in this scenario are far more smooth. This is because the yaw speed, nominator in ICR expression, is higher and much more steady. The means of the ICR locations are 0.404m , -1.738m , and 0.130m respectively. The ICR location of the right wheel is up to -2m , which means the right wheel is under critical slipping. The ICR location of the left wheel is smaller than the initial value of 0.435m that indicates that the left wheel is under skidding. Fig. 20 presents the wheel slip rate during steering. Take regardless of some pikes, the slip rate of the left wheel is almost 100 percent meaning that the left wheel is totally skidding. Additionally, the slip rate of the right wheel is about 65% and the sideslip angle is up to 40 degrees.

$$\begin{bmatrix} X_k^{ICR} \\ Y_k^{ICR} \\ \varphi_k^{ICR} \end{bmatrix} = \begin{bmatrix} X_k + v_{x,k+1}^{ICR} \cos(\varphi_k + \dot{\theta}_{k+1}^{ICR} \Delta T) \Delta T + v_{y,k+1}^{ICR} \sin(\varphi_k + \dot{\theta}_{k+1}^{ICR} \Delta T) \Delta T \\ Y_k + v_{x,k+1}^{ICR} \sin(\varphi_k + \dot{\theta}_{k+1}^{ICR} \Delta T) \Delta T - v_{y,k+1}^{ICR} \cos(\varphi_k + \dot{\theta}_{k+1}^{ICR} \Delta T) \Delta T \\ \varphi_k + \dot{\theta}_{k+1}^{ICR} \Delta T \end{bmatrix}$$

$$\begin{bmatrix} v_{x,k+1}^{ICR} \\ v_{y,k+1}^{ICR} \\ \dot{\theta}_{k+1}^{ICR} \end{bmatrix} = \mathbf{A}_{ICR} \mathbf{r} \begin{bmatrix} \omega_{l,k+1}^{en} \\ \omega_{r,k+1}^{en} \end{bmatrix}$$

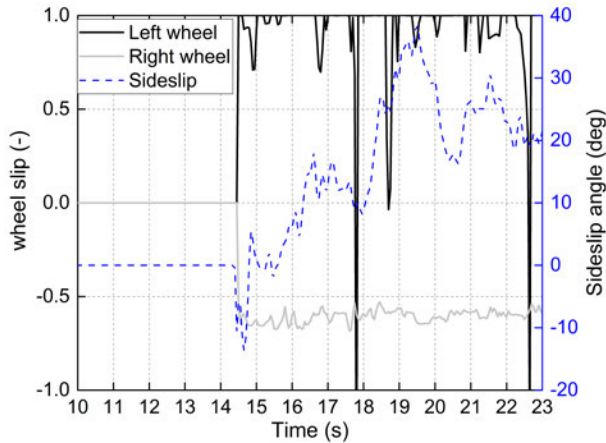


FIGURE 20. Wheel slip rate of the robot during driving on a curved path with small radius.

TABLE 2. Estimation error of robot’s position.

Scenario	En-DR	ICR	UKF+ICR	MI-UKF
1	4.886m	1.041m	0.109m	0.104m
2	14.695m	5.850m	0.701m	0.677m
3	0.224m	0.139m	0.017m	0.014m

In general, the performance in position estimates is evaluated by root-mean-square errors (RMS). The GNSS position is regarded as the reference to calculate the position error of each method. The RMS values of these algorithms in the three scenarios are listed in Table 2. It can be seen that the ICRs-based model achieves about 80% RMS reduction compared to the idealized DR odometry. Comparative refinement is shown when the GNSS position correction is available. By comparing the RMS values of ‘MI-UKF’ and ‘UKF+ICR’, about 10% error reduction is achieved.

VI. CONCLUSION AND FUTURE WORK

This paper presents a Multi-innovation UKF estimator designed for skid-steered mobile robots navigating in off-road environment. On the basis of the ICR model, we develop a slip-aware kinematic model for a four-wheeled SSMR. By merging the historical innovations into the UKF process, the introduced MI-UKF estimator is built. The position, orientation, velocity, and wheel slips of the mobile robot

DUBHE are estimated by fusing GNSS, IMU, and Encoder data.

In the field experiments, we design three test scenarios covering a high cruise speed of 4m/s, long distance of 100m, and large sideslip angle up to 40 degrees. By comparing the results of GNSS and Encoder, severe wheel slip can be found. The significant improvement conducted by ICR model can be seen by comparing the ‘ICR’ trajectory with ‘En-DR’ trajectory. And the improvement conducted by multi-innovation is obvious by comparing the ‘MI-UKF’ result and ‘UKF’ result. What is more, it is also shown that the ICR model performs better in mapping the wheel slip/skid in turning maneuver.

Even though MI-UKF shows some improvements in motion estimation, the application in discontinuous state space needs further investigation. Furthermore, computational burden could be another important problem that should be considered. For future work, vision-based sensors will be integrated into the multi-sensor fusion scheme. To reduce the computational burden, partial-linear system and some methods such as marginalized UKF is worthy to be explored and tested.

APPENDIX

The $\mathbf{h}(\mathbf{x}_{k+1})$ and the measurement noise vector \mathbf{v}_{k+1} in Section III can be written as follows,

$$\mathbf{h}(\mathbf{x}_{k+1}) = (X_{k+1}, Y_{k+1}, \varphi_{k+1}, v_{x,k+1}, v_{y,k+1}, \dot{\theta}_{k+1}, X_{k+1}, Y_{k+1}, \varphi_{k+1}, v_{x,k+1}, v_{y,k+1}, \dot{\theta}_{k+1})^T$$

$$\mathbf{v}_k = (0.3, 0.3, 0.3, 0.01, 0.01, 0.01, 0.5, 0.5, 0.5, 0.02, 0.02, 0.02)^T$$

where, the value of measurement noise vector is calculated regarding to the sensors’ specifications.

The position and velocity measurement vectors generated by encoder are written as $X_k^{ICR}, Y_k^{ICR}, \varphi_k^{ICR}$ and $v_{x,k+1}^{ICR}, v_{y,k+1}^{ICR}, \dot{\theta}_{k+1}^{ICR}$ shown at the top of this page.

REFERENCES

- [1] S. Al-Milli, K. Althoefer, and L. D. Seneviratne, “Dynamic analysis and traversability prediction of tracked vehicles on soft terrain,” in *Proc. IEEE Int. Conf. Netw., Sens. Control*, Apr. 2007, pp. 279–284.
- [2] J. Ni, J. Hu, and X. Li, “Dynamic modelling, validation and handling performance analysis of a skid-steered vehicle,” *Proc. Inst. Mech. Eng. D, J. Automobile Eng.*, vol. 230, no. 4, pp. 514–526, Jun. 2015.
- [3] D. M. Helmick, Y. Cheng, D. S. Clouse, L. H. Matthies, and S. I. Roumeliotis, “Path following using visual odometry for a mars rover in high-slip environments,” in *Proc. IEEE Aerosp. Conf.*, vol. 2, Mar. 2004, pp. 772–789.

- [4] E. Lucet, C. Grand, D. Salle, and P. Bidaud, "Dynamic yaw and velocity control of the 6WD skid-steering mobile robot RobuROC6 using sliding mode technique," in *Proc. IEEE/RJS Int. Conf. Intell. Robots Syst.*, Oct. 2009, pp. 4220–4225.
- [5] V. Rajagopalan, C. Mericli, and A. Kelly, "Slip-aware model predictive optimal control for path following," in *Proc. IEEE Int. Conf. Robot. Autom. (ICRA)*, May 2016, pp. 4585–4590.
- [6] C. Ordonez, N. Gupta, B. Reese, N. Seegmiller, A. Kelly, and E. G. Collins, "Learning of skid-steered kinematic and dynamic models for motion planning," *Robot. Auto. Syst.*, vol. 95, pp. 207–221, Sep. 2017.
- [7] Z. Zhao, H. Liu, H. Chen, J. Hu, and H. Guo, "Kinematics-aware model predictive control for autonomous high-speed tracked vehicles under the off-road conditions," *Mech. Syst. Signal Process.*, vol. 123, pp. 333–350, May 2019.
- [8] Z. B. Song, L. D. Seneviratne, K. Althoefer, X. J. Song, and Y. H. Zweiri, "Slip parameter estimation of a single wheel using a non-linear observer," *Robotica*, vol. 27, no. 6, pp. 801–811, Oct. 2009.
- [9] S. Thrun, "Probabilistic algorithms in robotics," *Ai Mag.*, vol. 21, no. 4, p. 93, 2000.
- [10] A. I. Eliazar and R. Parr, "Learning probabilistic motion models for mobile robots," in *Proc. 21st Int. Conf. Mach. Learn. (ICML)*, 2004, p. 32.
- [11] M. Sutoh, Y. Iijima, Y. Sakakieda, and S. Wakabayashi, "Motion modeling and localization of skid-steering wheeled rover on loose terrain," *IEEE Robot. Autom. Lett.*, vol. 3, no. 4, pp. 4031–4037, Oct. 2018.
- [12] J. L. Martínez, A. Mandow, J. Morales, S. Pedraza, and A. García-Cerezo, "Approximating kinematics for tracked mobile robots," *Int. J. Robot. Res.*, vol. 24, no. 10, pp. 867–878, Jul. 2005.
- [13] J. L. Martínez, J. Morales, A. Mandow, S. Pedraza, and A. Garcia-Cerezo, "Inertia-based ICR kinematic model for tracked skid-steer robots," in *Proc. IEEE Int. Symp. Saf., Secur. Rescue Robot. (SSRR)*, Oct. 2017, pp. 166–171.
- [14] A. Mandow, J. L. Martínez, J. Morales, J. L. Blanco, A. Garcia-Cerezo, and J. Gonzalez, "Experimental kinematics for wheeled skid-steer mobile robots," in *Proc. IEEE/RJS Int. Conf. Intell. Robots Syst.*, Oct. 2007, pp. 1222–1227.
- [15] T. Wang, Y. Wu, J. Liang, C. Han, J. Chen, and Q. Zhao, "Analysis and experimental kinematics of a skid-steering wheeled robot based on a laser scanner sensor," *Sensors*, vol. 15, no. 5, pp. 9681–9702, Apr. 2015.
- [16] H. Lu, G. Xiong, and K. Guo, "Motion predicting of autonomous tracked vehicles with online slip model identification," *Math. Problems Eng.*, vol. 2016, Sep. 2016, Art. no. 6375652.
- [17] S. Rabiee and J. Biswas, "A friction-based kinematic model for skid-steer wheeled mobile robots," in *Proc. Int. Conf. Robot. Autom. (ICRA)*, May 2019, pp. 8563–8569.
- [18] J. Yi, J. Zhang, D. Song, and S. Jayasuriya, "IMU-based localization and slip estimation for skid-steered mobile robots," in *Proc. IEEE/RJS Int. Conf. Intell. Robots Syst.*, Oct. 2007, pp. 2845–2850.
- [19] J. Yi, H. Wang, J. Zhang, D. Song, S. Jayasuriya, and J. Liu, "Kinematic modeling and analysis of skid-steered mobile robots with applications to low-cost Inertial-measurement-unit-based motion estimation," *IEEE Trans. Robot.*, vol. 25, no. 5, pp. 1087–1097, Oct. 2009.
- [20] C. B. Low and D. Wang, "Integrated estimation for wheeled mobile robot posture, velocities, and wheel skidding perturbations," in *Proc. IEEE Int. Conf. Robot. Autom.*, Apr. 2007, pp. 2355–2360.
- [21] C. C. Ward and K. Iagnemma, "A dynamic-model-based wheel slip detector for mobile robots on outdoor terrain," *IEEE Trans. Robot.*, vol. 24, no. 4, pp. 821–831, Aug. 2008.
- [22] F. Rogers-Marcovitz, M. George, N. Seegmiller, and A. Kelly, "Aiding off-road inertial navigation with high performance models of wheel slip," in *Proc. IEEE/RJS Int. Conf. Intell. Robots Syst.*, Oct. 2012, pp. 215–222.
- [23] J. Pentzer, S. Brennan, and K. Reichard, "Model-based prediction of skid-steer robot kinematics using online estimation of track instantaneous centers of rotation," *J. Field Robot.*, vol. 31, no. 3, pp. 455–476, Mar. 2014.
- [24] M. A. Javed, W. Owen, M. Biglarbegan, and W. Melek, "A hybrid EKF/KF state estimator for a skid-steered ATV," *Vehicle Syst. Dyn.*, vol. 52, no. 1, pp. 85–110, Nov. 2014.
- [25] C. Wang, W. Lv, X. Li, and M. Mei, "Terrain adaptive estimation of instantaneous centres of rotation for tracked robots," *Complexity*, vol. 2018, pp. 1–10, Nov. 2018.
- [26] W. Lv, J. Chang, Y. Kang, Y.-B. Zhao, and Z. Li, "Terrain vision aided online estimation of instantaneous centers of rotation for skid-steering mobile robots," in *Proc. IEEE 8th Annu. Int. Conf. CYBER Technol. Autom., Control, Intell. Syst. (CYBER)*, Jul. 2018, pp. 516–521.
- [27] M. Partovibakhsh and G. Liu, "Adaptive unscented Kalman filter-based online slip ratio control of wheeled-mobile robot," in *Proc. Proc. 11th World Congr. Intell. Control Autom.*, Jun. 2014, pp. 6161–6166.
- [28] H. Fang, N. Tian, Y. Wang, M. Zhou, and M. A. Haile, "Nonlinear Bayesian estimation: From Kalman filtering to a broader horizon," *IEEE/CAA J. Automatica Sinica*, vol. 5, no. 2, pp. 401–417, Mar. 2018.
- [29] J. Chen, G. Jia, C. Yang, L. Li, X. Ran, and J. Song, "UKF-based adaptive variable structure observer for vehicle sideslip with dynamic correction," *IET Control Theory Appl.*, vol. 10, no. 14, pp. 1641–1652, Sep. 2016.
- [30] Z. Liu, X. Dang, and B. Jing, "A novel open circuit voltage based state of charge estimation for lithium-ion battery by multi-innovation Kalman filter," *IEEE Access*, vol. 7, pp. 49432–49447, 2019.
- [31] Z. Ke and S. Ying, "Steady-state Kalman fusion filter based on improved multi-innovation least squares algorithm," in *Proc. 37th Chin. Control Conf. (CCC)*, Jul. 2018, pp. 4434–4437.
- [32] F. Ding and T. Chen, "Performance analysis of multi-innovation gradient type identification methods," *Automatica*, vol. 43, no. 1, pp. 1–14, Jan. 2007.
- [33] M. Gan, X.-X. Chen, F. Ding, G.-Y. Chen, and C. L. P. Chen, "Adaptive RBF-AR models based on multi-innovation least squares method," *IEEE Signal Process. Lett.*, vol. 26, no. 8, pp. 1182–1186, Aug. 2019.
- [34] L. Xu, F. Ding, Y. Gu, A. Alsaedi, and T. Hayat, "A multi-innovation state and parameter estimation algorithm for a state space system with d-step state-delay," *Signal Process.*, vol. 140, pp. 97–103, Nov. 2017.
- [35] F. Liu, J. Zhou, J. Chen, and X. Yin, "An approach of trajectory estimation for high-speed unmanned skid-steered vehicle," in *Proc. DESTech Trans. Environ., Energy Earth Sci.*, Feb. 2018, pp. 1–6.
- [36] B.-C. Chen and F.-C. Hsieh, "Sideslip angle estimation using extended Kalman filter," *Vehicle Syst. Dyn.*, vol. 46, pp. 353–364, Sep. 2008.
- [37] W. Lv, Y. Kang, and J. Qin, "Indoor localization for skid-steering mobile robot by fusing encoder, gyroscope, and magnetometer," *IEEE Trans. Syst., Man, Cybern. Syst.*, vol. 49, no. 6, pp. 1241–1253, Jun. 2017.
- [38] S. Xie, D. Chen, X. Chu, and C. Liu, "Identification of ship response model based on improved multi-innovation extended Kalman filter," *J. Harbin Eng. Univ.*, vol. 39, no. 2, pp. 282–289, Feb. 2018.
- [39] Z. Liu, J. Guo, L. Ding, H. Gao, T. Guo, and Z. Deng, "Online estimation of terrain parameters and resistance force based on equivalent sinkage for planetary rovers in longitudinal skid," *Mech. Syst. Signal Process.*, vol. 119, pp. 39–54, Mar. 2019.
- [40] B. Sebastian and P. Ben-Tzvi, "Support vector machine based real-time terrain estimation for tracked robots," *Mechatronics*, vol. 62, Oct. 2019, Art. no. 102260.
- [41] Y. Hori, Y. Toyoda, and Y. Tsuruoka, "Traction control of electric vehicle: Basic experimental results using the test EV 'UOT electric march,'" *IEEE Trans. Ind. Appl.*, vol. 34, no. 5, pp. 1131–1138, Sep. 1998.
- [42] G. Chang, "Marginal unscented Kalman filter for cross-correlated process and observation noise at the same epoch," *IET Radar, Sonar Navigat.*, vol. 8, no. 1, pp. 54–64, Jan. 2014.
- [43] G. Chang, "Loosely coupled INS/GPS integration with constant lever arm using marginal unscented Kalman filter," *J. Navigat.*, vol. 67, no. 3, pp. 419–436, Dec. 2013.



FANGXU LIU was born in Chongqing, China, in 1996. He received the B.S. degree in vehicle engineering from the Beijing Institute of Technology, in 2017, where he is currently pursuing the master's degree with the National Key Laboratory of Vehicular Transmission.

His research interests include motion estimation, prediction, and tracking control for unmanned ground vehicles and mobile robots navigating in off-road environment. Specifically, he focuses on the application of multisensor fusion methods, online learning, and adaptive model predictive control in autonomous driving.



XUEYUAN LI received the B.S., M.S., and Ph.D. degrees in vehicle engineering from the Beijing Institute of Technology, Beijing, China, in 1999, 2002, and 2010, respectively.

He was the Director of the National Key Laboratory of Vehicular Transmission, from 2008 to 2014. He is currently the Vice Director of the Department of Vehicle Engineering, Beijing Institute of Technology. Since 2002, he has been an Associate Professor with the School of Mechanical Engineering, Beijing Institute of Technology. His research interests include vehicle transmission theory and technology, unmanned vehicle theory and technology, and skid-steered vehicle dynamics.



WEI LAN received the B.S. degree in computer science and technology from the Beijing Institute of Technology, Beijing, China, in 2006. Since 2006, he has been an Associate Researcher with the China North Vehicle Research Institute, Beijing. His research interests include unmanned platform design and integration, motion and propulsion control, and remoted operation of unmanned ground vehicle.

• • •



SHIHUA YUAN received the B.S., M.S., and Ph.D. degrees in vehicle engineering from the Beijing Institute of Technology, Beijing, China, in 1982, 1985, and 2000, respectively.

From 1992 to 1997, he was an Associate Professor with the Beijing Institute of Technology, where he has been a Professor with the School of Mechanical Engineering, since 1997. He is the author of more than 100 research articles. His research interests include vehicle dynamics, vehicle braking energy recovery, vehicle continuous transmission and its control technology, and unmanned ground vehicle.